Probing Multiscale Structure and Dynamics of Waxy Crude Oil by Low-Field NMR, X-ray Scattering, and Optical Microscopy

Imane Yalaoui, Thibaud Chevalier, Pierre Levitz, Myriam Darbouret, Thierry Palermo, Guillaume Vinay, Loïc Barré

Probing multi-scale structure and dynamics of waxy crude oil by low field NMR, X-Ray scattering and optical microscopy

Imane Yalaoui [1,2,4], Thibaud Chevalier[2*], Pierre Levitz[1], Myriam Darbouret[3], Thierry Palermo [4], Guillaume Vinay[2] and Loïc Barré [2*]*

[1]Sorbonne Université, CNRS, UMR 8234, Physicochimie des Electrolytes et Nanosystèmes Interfaciaux, 4 place Jussieu, 75005 Paris, France

[2]IFP Energies Nouvelles, 1 et 4 avenue de Bois-Préau, 92852 Rueil-Malmaison, France

[3]IFP Energies nouvelles, Rond-point de l'échangeur de Solaize, BP 3, 69360 Solaize, France

[4]Total S.A, Research and Development Flow Assurance, CSTJF-Avenue Larribau, 64018 Pau Cedex

Corresponding author

*E-mail: imane.yalaoui@ifpen.fr, loic.barre@ifpen.fr, thibaud.chevalier@ifpen.fr

Keywords: Cross Polarized Microscopy, NMR, X-ray Scattering, waxy oil, wax, *n*-paraffins crystallization, bulk

ABSTRACT

Wax deposition is one of the major concern for waxy crude oil production and transportation. A better understanding and prediction of fluid properties related to this issue requires knowledge of the medium structuration at scales ranging from nanometers (molecules) to a few micrometers (crystals). For this purpose, the behavior of a waxy crude oil in bulk was compared to a model oil over a wide range of temperatures above and below the Wax Appearance Temperature (WAT). The combined use of Cross Polarized Microscopy (CPM) and the implementation of innovative techniques for the field such as SAXS/WAXS and low field NMR has provided a more precise idea of the structure of these two types of fluids. If the nature of the orthorhombic crystals and their lamellar shape are identical for both fluids, a very appreciable difference is highlighted in their chain axis dimensions. The *n*-paraffins crystals size is larger than 120 nm in the model oil. In the crude oil, it is only about 1-10 nm with a long range order in the directions perpendicular to the chain axis and a monomolecular thickness in the chain axis. Moreover, from the model oil CPM images, we observed aggregates of lamellar shape crystals. Since the model oil does not contain asphaltenes and resins, the crystals are larger and the branches divide significantly less than in the crude oil which results in a trapped liquid protons population unobservable in the model oil. All these observations give a vision of the structure of *n*-paraffins crystals. It is made of aggregates of relatively dense lamellae in the center and more aerated lamellae at the periphery which split into several branches.

1. INTRODUCTION

Production and transportation of waxy crude oils through long pipelines at low temperatures is a critical challenge in deep and ultra-deep offshore. Waxy crude oils are complex mixtures containing paraffins, aromatics, naphthenes, resins and asphaltenes with a carbon number higher than 20 [1]. At high temperatures, the *n*-paraffins (waxes) remain dissolved in crude oil but when the temperature at the pipe wall drops below the Wax Appearance Temperature (WAT), the crude oil *n*-paraffins start to crystallize and cause serious issues such as wax deposition on the walls of pipelines[2–4], an increase of the waxy crude oil viscosity leading to a non-Newtonian behavior[5–7] and restart issues of the pipelines due to the waxy gelation during shutdowns[8–10]. These problems lead to significant additional production costs[11] and the development of operational remediation techniques such as pigging or chemical inhibition requires a deep understanding of the complex behavior of waxy crude oils. In order to reproduce the flow of crude oil in pipelines, flow loop experiments are carried out in the laboratory and require the knowledge of the properties of *n*-paraffins crystals aggregates such as structure, size of unit crystals, fluid behavior in aggregates ...). Indeed, knowing these properties enable a better characterization of wax deposit structure and a deeper understanding of the different mechanisms that lead to wax deposit formation.

The literature presents numerous studies performed in order to probe the structure of the deposit in which classical characterization techniques have been used. These techniques include rheology[11,12,13], DSC[11,12,14], HTGC[11,15–17] and densimetry[6]. They allow the determination of the waxy oils main properties such as viscosity, density, WAT, Pour Point, distribution and the *n*-paraffins content. These fundamental characterizations are important for the development of

models predicting wax deposit formation and flow properties but do not allow a multi-scale description of the deposit structure.

To investigate the morphology and size of crystals in crude oils, optical microscopy has been widely used but, depending on the experimental conditions set-up, different sizes and morphologies have been found [14,18–20].

Slightly more advanced techniques have been implemented for waxy oils characterization. NMR relaxometry has been used to characterize waxy crude oils and in particular to determine the *n*-paraffins content in crude oils and their distributions [21,22]. Furthermore, NMR relaxometry has also been used to understand the role of inhibitors on wax crystallization[23]. X-ray diffraction has been used to study the structural behavior of pure *n*-paraffins or model oils, but few studies have been carried out directly on the crude oils[24–26]. Indeed, binary, ternary, quaternary mixtures or model oils have been used mainly because of their simplified structure compared to real crude oils. However, these studies are still far from real complex systems.

In the present paper, we propose to make a description of the structure of a waxy crude oil at multi length-scale (1 Å to 10 µm) in both model oil and crude oil using a variety of analytical techniques such as Cross Polarized Microscopy (CPM)[19,27–29], Small and Wide angle X-ray scattering (SAXS/WAXS)[30–32] and low field NMR[33,34]. Each technique provides useful information to finely describe the structural behavior of *n*-paraffins crystals in a model and a crude oil: CPM makes the visualization of the *n*-paraffins crystals possible, SAXS/WAXS provides information on crystals inter-arrangement, their size and shape and NMR can be used to study fluid dynamics within the formed crystal network.

2. MATERIALS AND METHODS

In this study, a model oil and a crude oil were used. The model oil allowed to simplify the application of CPM and to evaluate its ability to represent a crude oil according to the observed behaviors.

2.1. Crude oil and model oil

The model oil was prepared using a disaromatized aliphatic oil (Hydroseal G250H (C_{15}-C_{20}), number C.A.S 64742-46-7, crystallization temperature -20 °C) density 0.812 g/cm^3 at 20 °C and 10 % weight of wax (commercial wax purchased from Prolabo, melting point 52-54 °C). The model oil WAT is 22°C, which is well suited to the different experimental set-ups we used. The waxy crude oil, which was provided by Total and coming from a Congo field, has a density of 35° API (American Petroleum Institute gravity) and a WAT of 51 °C. The crude oil was filtrated with a filter size of 5 µm at 60 °C in order to get rid of all solid particles such as sand particles.

Before the beginning of each experiment, samples were heated at a temperature above the WAT (WAT+20°C) during few hours and were hand-mixed during approximately 1 minute.

The WAT and the weight fraction of wax crystals C_{wax} (wt.%) of the oils were obtained with a differential scanning calorimeter (DSC). The detailed procedure is described in supplementary information **a**. Volume fractions ϕ (where $\phi = V_s/(V_s + V_L)$ with V_s as being the solid volume and and V_L the liquid volume) were obtained from C_{wax} and densities of the suspending liquid phase ρ_L (supplementary information **b**) and solid wax ρ_{wax}. According to the literature, between nC$_{20}$ and nC$_{32}$, the density of the solid phase varies slightly and linearly between[31] 0.92 g/cm^3 and 0.93 g/cm^3. Since it is known that a *n*-paraffins mixture produces a solid solution that contains

defects, then the density of the mixture will be lower than that of the pure phase of *n*-paraffins which constitutes the mixture [35]. Thus, we assumed that the density of the solid wax in the mixtures[6,36] ρ_{wax} is about 0.9 g/cm^3.

A SARA analysis was performed on the crude oil in order to know its composition (**Table 1**).

Table 1. *Composition of the crude oil.*

Components	Content, % mass
C_6-C_{14}	25.8
Saturated C_{14+}	49.7
Aromatics C_{14+}	7.6
Resins	13.2
Asphaltenes	3.6

The *n*-paraffins distribution of the crude oil and the commercial wax are shown in **Figure 1.** The *n*-paraffins distribution of the commercial wax was obtained by High Temperature Gas Chromatography (HTGC) with an Agilent 6890 gas chromatograph. HTGC is commonly used to determine the *n*-paraffins distributions in crude oils and its products[15,16,37]. The *n*-paraffins distribution in the crude oil was obtained by performing GC analysis with a Thermo Scientific Trace 1300 gas chromatograph on the fraction which does not contain heavy resins and asphaltenes (obtained by SARA separation). The *n*-paraffins distribution of the commercial wax covers 13 *n*-alkanes ranging from C_{21} to C_{34} and carbon distribution of the crude oil had a range from C_7 to C_{40+}. The *n*-paraffins proportion was quantified from C_7 to C_{40} ant it is approximately 26 weight %. A simulated distillation analysis by HTGC was also carried out on the crude oil and showed that the distribution of *n*-paraffins extends to over 86 carbon atoms. However, it was not possible to quantify them. The *n*-paraffins distribution is characterized by its mean number of

carbon atoms $\bar{n}$ and the standard deviation σ. These parameters were calculated from relationships [26,38] described in supplementary information **d**.

The characteristics of the *n*-paraffins distributions in the model oil and crude oil (only from C_7 to C_{40}) are summarized in **Table 2**. For the crude oil, since we do not have the complete distribution we could not determine $\bar{n}$ and we can only calculate a minimum value of σ.

Table 2. *Characteristics of the crude oil and model oil n-paraffins distributions.*

Sample	Composition in *n*-paraffins	*n*-paraffins content	$\bar{n}$	σ
Crude oil	C_7H_{16} to $C_{40}H_{82}^+$	> 26 wt. %	-	>7.2
Model oil	$C_{21}H_{44}$ to $C_{34}H_{70}$	10 wt. %	24.8	2.1

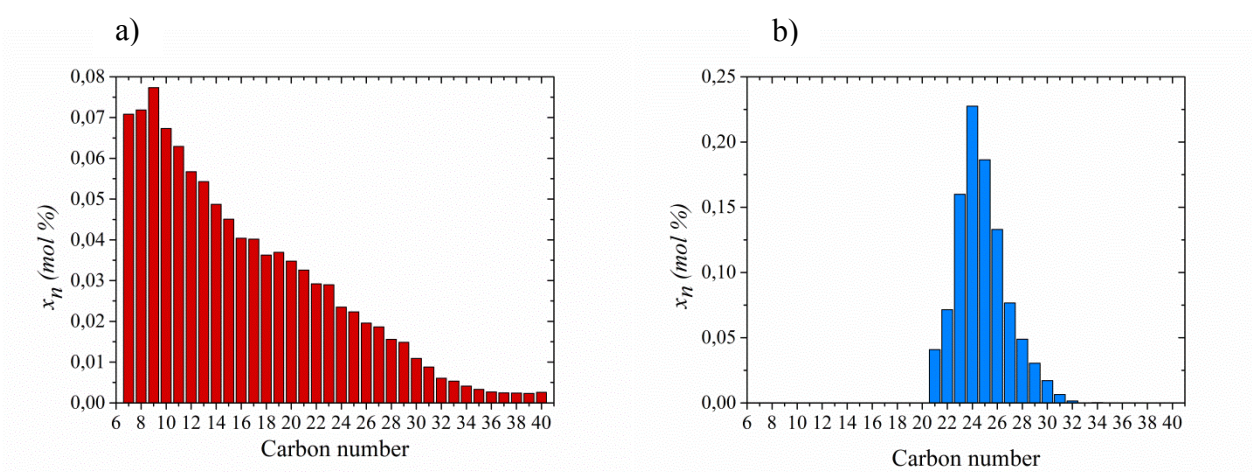

Figure 1. *n-paraffins molar distributions in a) the crude oil (from C_7 to C_{40}) and b) the model oil.*

According to the GC, the minimum mass of paraffin contained in the crude oil is 26 weight %. We considered this value to be the total mass of *n*-paraffins in the sample to calculate C_{wax} as described in supplementary information **a**. C_{wax} of the two oils are shown in **Figure 2**.

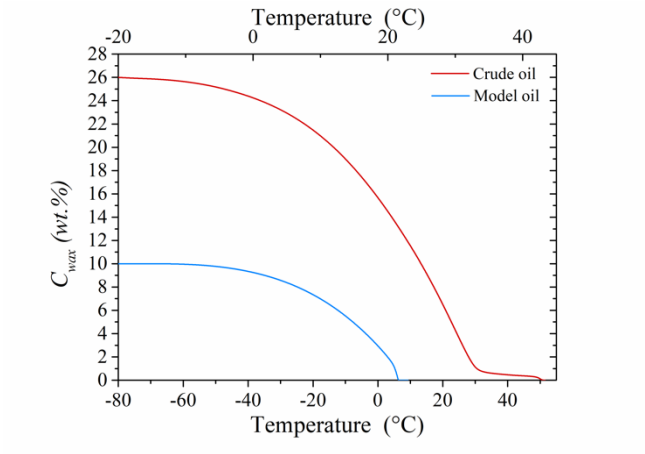

Figure 2. *Evolution of the mass fraction of wax crystals C_{wax} in the crude oil from 45°C to – 80 °C (bottom X axis) and the model oil (top X axis) from 20°C to – 20 °C.*

2.2. Liquid separation from the solid/liquid gelled mixture by temperature-controlled centrifugation

To better understand the liquid phase behavior during the crystallization process, the liquid phase was extracted at various temperatures from the solid/liquid gelled mixture using a temperature-controlled centrifugation method at five different temperatures. Indeed, this method allows to separate the liquid phase from the *n*-paraffins crystals and to study its composition. The experimental protocol is described in supplementary information **e**. After the experiments, five centrifuged crude oils with different WAT were obtained (**Table 3**). Their compositions are given in supplementary information **c**.

Table 3. *Centrifuged oils samples obtained at different temperatures with their associated WAT.*

	Oil 40	Oil 20	Oil 5	Oil 0	Oil -5
WAT (°C)	32.7	15.1	1.3	-3.4	-9.7

2.3. Cross Polarized Microscopy (CPM)

CPM was used to visualize directly the size and the shape of wax crystals. CPM imaging was performed with an Olympus BH2 UMA microscope, which was fitted with cross-polarization filters and an Axiocam 305 color camera. Temperature and cooling rate were controlled by a LNP95 Linkam. The samples were preheated, filled into glass capillaries with a cross section of 0.2 mm x 4 mm and were sealed on both ends using glue. We recorded two images, using different objectives (×10, ×20), to compare the wax crystals sizes obtained respectively for the crude oil and for the model oil. During measurements, the temperature was first ramped up to 70 °C (crude oil) or 40 °C (model oil), kept constant for 5 minutes and then decreased down to 0 °C (crude oil) or 18 °C, 5 °C and -10 °C (model oil) at a rate of -10 °C/min. The temperature was held constant at 0 °C or 18 °C, 5 °C and 10 °C and images were taken during the isothermal period.

2.4. Low field Nuclear Magnetic Resonance (NMR) [39,40]

During the crystallization of *n*-paraffins, the network of crystals formed in the liquid medium can be shown as a porous network (also referred as a crystals network). This porous network consists of distinct pores which contains the liquid that is more or less confined during crystallization. NMR is a non-destructive technique that allowed us to get indirect information about the pore sizes and the behavior of the liquid within the pores using the T_2 relaxation time distribution.

NMR experiments were conducted on a low field (MQR GeoSpec core analyzers: 20 MHz) Oxford Instrument spectrometer equipped with a 18 mm diameter probe. To acquire the transverse relaxation time (T_2) decay, a modified Carl-Purcell-Meiboom-Gill (CPMG) sequence was used: the inter echo spacing (2τ) varies from 100 µs to 300 µs and the number of echoes acquired was set to 20 000. The T_2 relaxation time distributions were calculated using the IFPEN

software MEA (Multi-Exponential-Analysis). Glass tubes suitable for the 18 mm NMR probe are filled with approximately 1 g of the fluid sample and then put in the NMR probe. Nitrogen was used to heat and cool the sample. To control the temperature of the sample, the spectrometer was connected to a VT (Variable Temperature) controller coupled with a FTS Low Temperature Cooling Systems & Equipment that allow us to performed measurements over a temperature range between 80 °C and -20 °C. The temperature is maintained by the circulation of a flow of air. To ensure that the sample temperature was stable, the evolution of the magnetization *M(t)*, as a function of time, was followed after several Hahn Echoes (a Hahn Echo is a CPMG sequence with one echo). The temperature of the sample was considered stable when the magnetization remains constant. The stabilization time was about 30-45 minutes. Each raw curve obtained was normalized by the mass of the sample in the glass tube.

In a homogenous B_0 field, we followed the magnetization decay *M(t)* in the plane transverse to the B_0 field, which is characterized by the relaxation time T_2. This characteristic time results essentially from liquid-solid interactions of the nuclear spins carried by molecules exploring the pore space by diffusion. Molecular diffusion leads to an exchange between the surface and bulk volumes.

Assuming uniform surface relaxivity and a rapid exchange between liquid and all crystals surfaces, the relaxation time T_2 can be expressed as[40]:

$$\frac{1}{T_2} = \frac{1}{T_{2B}} + \rho_2 \left[\frac{S}{V}\right]_{NMR} \quad (1)$$

Where T_{2B} is the transversal relaxation time of the bulk liquid, V and S are respectively the volume and the surface of the total pore space. ρ_2 is the surface relaxivity or the relaxation velocity at the pore surface. For a uniform pore network, the volume to surface $[V/S]_{NMR}$ ratio gives an estimation of the pore size.

In the presence of a distribution of pore sizes, and in the regime of fast molecular exchange bulk-surface in each pore but not between pores, the measured magnetization decay *M(t)* is analyzed in term of a discrete series of exponential decays such as:

$$M(t) = \sum_i A_i \exp\left(-\frac{t}{T_{2i}}\right) \tag{2}$$

Where A_i is the normalized number of spins associated with a relaxation time T_{2i}. The T_2 relaxation time distributions are obtained by plotting a curve $A(T_2)$. The total magnetization $M(t=0)$ represents the total amount of spins. In practice, it is possible to detect only the spins that have a sufficiently long relaxation time: this is the case of the bulk liquid. On the contrary, for solids, relaxation times are very short and the detection of the magnetization associated with these spins will depend on the spectrometer and its characteristics. For example, during our CPMG measurements performed at 20 MHz we cannot detect the magnetization associated with *n*-paraffins crystals, which have a relaxation time T_2 of 70 µs [21]. $M(t=0)$ varies according to the inverse of temperature. To correct the effects related to temperature variation, the measured magnetization is corrected by the Curie's law.

2.5. Small and Wide Angle X-ray scattering (SAXS/WAXS)

SAXS/WAXS were used to investigate the crystallographic structure of *n*-paraffins crystals, their form, size and number density, their surface area as well as their spatial correlation at larger length scale. SAXS/WAXS experiments were performed at IFPEN. The experimental set-up is equipped with a copper rotating anode (Rigaku MM07) providing a X-ray beam with a wavelength of λ = 1.5418 Å. When the beam crosses the sample, a small part is scattered and is captured simultaneously by a SAXS and WAXS two-dimensional (2D) detectors (respectively Rigaku and Xenocs). This design allows to collect scattering intensities over a large range of

213 scattering angles 2θ. Each pixel coordinate was converted to wave vector q thanks to
214 measurement of standards, namely Ag Behenate and LaB_6 respectively for SAXS and WAXS[41].
215 The scattering vector q is defined as $q = \frac{4\pi sin(\theta)}{\lambda}$, with θ being half the deviation angle, and
216 corresponds to an inverse correlation length probed. In the case of a periodic structure, a value of
217 q in the reciprocal space is related to a repeating distance d in the real space by the Bragg law: d
218 $= 2\pi/q$. For experiments, working with two different distances between sample and detectors
219 allows to cover a total q domain of almost three decades ranging from 6 10^{-3} $Å^{-1}$ up to 4.3 $Å^{-1}$.
220 SAXS and WAXS experiments were carried out simultaneously on the same sample volume.
221 The crude oil and the model oil were preheated and filled into glass capillaries with a diameter of
222 1.5 mm, which were flame-sealed on both ends. Capillaries were then placed on the Linkam
223 temperature-controlled sample holder and heated for a few minutes to 70 °C (crude oil) or 50 °C
224 (model oil) before the measurements begin. The whole stage was placed in a vacuum chamber to
225 avoid any condensation or frost on wall capillaries upon cooling. Then, the temperature was
226 cooled down at 10 °C/min from 70 °C to -70 °C or from 50 °C down to -20 °C. The raw
227 scattered intensities were normalized by the thickness of the sample, the transmission and the
228 measuring time. Empty capillary as well as liquid intensities, obtained from Hydroseal or
229 centrifuged oils above their WAT, were subtracted to each measurement according to their
230 volume fraction. Finally, Lupolen was chosen as calibration standard[42] to convert intensities in
231 absolute units (cm^{-1}).

232 For a two-phase system made of monodisperse particles distributed in space, the general
233 equation describing the scattered intensity of particles in the solvent can be written as:
234

$$I(q) = N_p \, \Delta\rho_{scat}{}^2 \, v^2 \, P(q) \, S(q) \quad (3)$$

Where N_p is the number density of scattering particles and v is the volume of one particle. N_p can be written as ϕ/v where ϕ is the particle volume fraction. P(q) is the form factor, which is a function of shape and size of particle [P(0)=1]. S(q) is the structure factor describing particles position correlation resulting from their mutual interactions. For concentrated systems, the structure factor provides significative structural information at length scale larger than the typical size R_G of scatterers, *i.e* at q values smaller than ~ R_G^{-1}. At q values much larger than R_G^{-1}, $S(q)$ tends to 1. $\Delta\rho_{scat}$ is a contrast term, which is the scattering length density difference between the particles and solvent.

The form factor P(q) can be expressed in different ways depending on the particles shapes and the q domain:

At large q values (q> 1/l), with l being the smallest dimension of the particle, known as the 'Porod' regime, it is possible to determine the total surface area developed by particles (S) in a given volume (V) using the following equation:

$$I\ (q \rightarrow \infty) = \Delta\rho^2\ \frac{2\pi}{q^4}\left[\frac{S}{V}\right]_{SAXS} \tag{4}$$

The surface to volume ratio $[S/V]_{SAXS}$ can also be written as:

$$\left[\frac{S}{V}\right]_{SAXS} = \frac{s}{v} \times \phi \tag{5}$$

Where s and v stand respectively for the surface area and the volume of one particle and ϕ is the particle volume fraction.

At intermediate q values, the variation of the scattering intensity $I(q)$ can follow a power law defined as:

$$I(q) \sim q^{-\alpha} \quad (6)$$

Where α is related to the dimensionality of the structure. In the dilute regime, $\alpha = 1$ for rods and 2 for lamellae or discs.

The size of crystalline domains S_{hkl} , in a direction perpendicular to a $h\ k\ l$ atomic plane, represent the size of 'perfect' crystal (without crystalline defects), they give a minimal value of the particle size in the considered direction. They are inferred from the full width at half maximum $FW(S)_{hkl}$ of the considered (hkl) Bragg reflection through the Scherrer relation described in supplementary information **g** .

3. RESULTS

3.1. Crystals observations

To get a first estimation of the *n*-paraffins particles form and size at the micrometric scale, CPM experiments were conducted. At high temperatures, only a homogeneous black background, corresponding to the solvent, is visible. When the sample is cooled and temperature falls below the WAT, bright white particles appear as a result of birefringent crystal formation. For the crude oil, the perceptible particles are small (size of a bright spot ≈ 1 µm) and it is difficult to have an accurate information about their size and shape (**Figure 3a**). On the contrary, for the model oil, it is easier to distinguish the different *n*-paraffins crystals and to determine their size and shape (**Figure 3b** and **Figure 3c**). Crystals appear in various orientations (**Figure 3b**), some of them being positioned flat or on the slice. They are thin platelets made up of a stack of lamellae with typical dimensions (150 µm length x 50 µm width x 5 µm thickness). The areas pointed by arrows in **Figure 3b** and **Figure 3c** shows the stacking of lamellae constituting the platelets. These lamellae seem to divide into several branches and form a less concentrated area of

lamellae (zoom **Figure 3b**). As the temperature decreases, the lamellae divide more and more into several branches and form a structure called hedrite (**Figure 3c** and **Figure 3d**). The hedrite-shaped structure is a structure observed during the crystallization of semi-crystalline polymers[43].

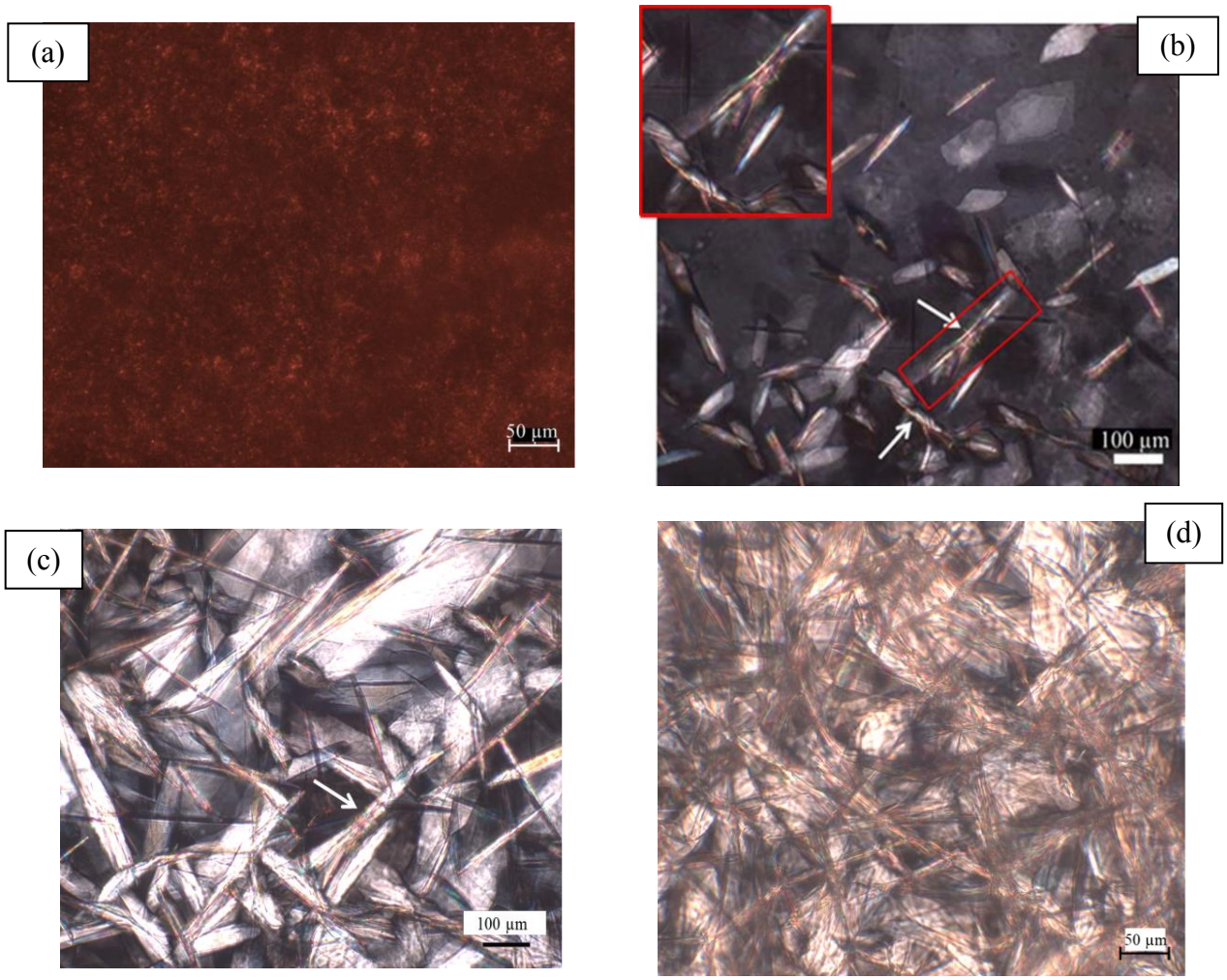

Figure 3. *CPM images obtained a) at 0°C (×20 magnification) for the crude oil (WAT = 51°C). For the model oil (WAT = 22°C) b) at 18 °C (×10 magnification) c) at 5 °C (×10 magnification) and d) at -10 °C (×20 magnification) after cooling down at -10 °C/min. The areas pointed by arrows represent the aggregate which is composed of a stack of crystals that divide into branches.*

3.2. From *n*-paraffins chains to crystals aggregates

To go further in the characterization of crystals, we now analyze SAXS/WAXS results. The 2D scattering patterns (images are not shown) obtained appears fully isotropic for the crude oil and slightly punctuated for the model oil. The punctuation of Bragg rings appears when all the crystals orientation in the probed volume are not equally probable. From CPM observations, we suspect that crystals in the model oil grew to such large size that some preferential orientation occurs. However, as the rings were quite homogeneous and almost isotropic, images were azimuthally averaged to obtain 1D curves.

In order to represent only the major evolutions and to allow a good readability of the results, we represent in **Figure 4** the recomposed 1D spectra, in the different *q* domains, obtained at only a few temperatures above and below the WAT. They are analyzed according to *(i)* their Bragg peak features ascribed to phase identification and crystal size domains and to *(ii)* their general behavior at small *q* values.

3.2.1. Crystalline structure

At wide angles, and above the WAT, the X-ray scattering spectra in **Figure 4** present a wide halo located at q = 1.31 $Å^{-1}$ ± 0.01 $Å^{-1}$ (d = 4.5 ± 0.03 Å). This halo is associated with the liquid phase. As expected, the halo area decreases below the WAT. When the temperature falls below the WAT, four narrow Bragg peaks appear, located at d = 4.1 Å ± 0.03 Å, d = 3.7 Å ± 0.02 Å, d = 3.1 Å ± 0.02 Å and d = 2.4 Å ± 0.01 Å. These peaks are respectively attributed to the *hk0* reflections, (110+111), (020), (120) and (200), of an orthorhombic crystal system[44,45]. The most intense one appears just at the WAT temperature, which confirms the sensitivity of X-ray scattering for the Wax Appearance Temperature determination[30].

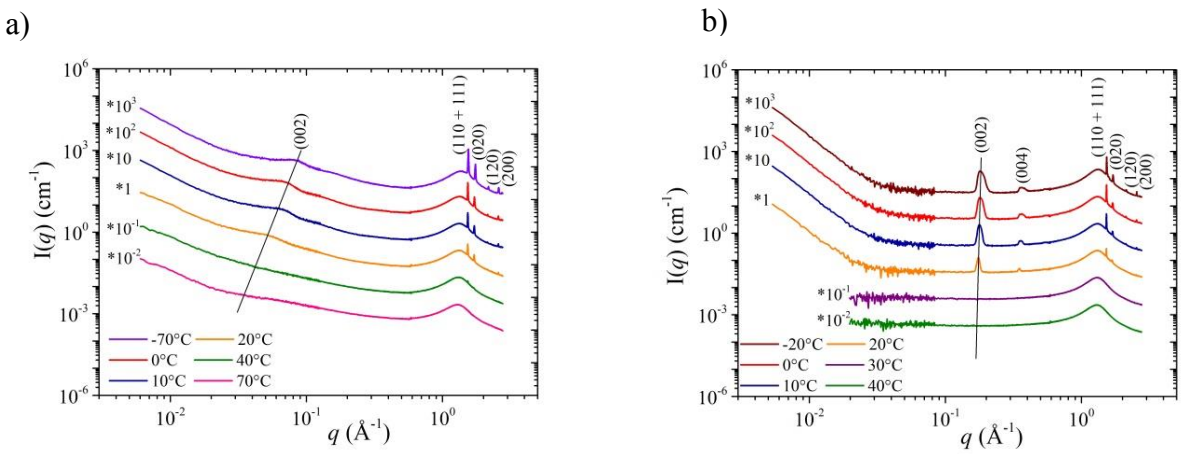

Figure 4. *X-ray scattering spectra at different temperatures before the solvent subtraction for a) the crude oil (WAT = 51 °C) and b) the model oil (WAT = 22 °C).*

The unit cell parameters *a* and *b* are inferred from peak positions and indexations using equation described in supplementary information **g**. For the two oils, these parameters slightly decrease with temperature (**Figure 5**). This small decrease is of the same order of magnitude than the one reported for pure alkanes samples[46], which remain in an ordered orthorhombic crystalline phase with no phase transition. There is no other Bragg peak appearance in the *q* domain under study, excluding the possibility of another low temperature phase transition.

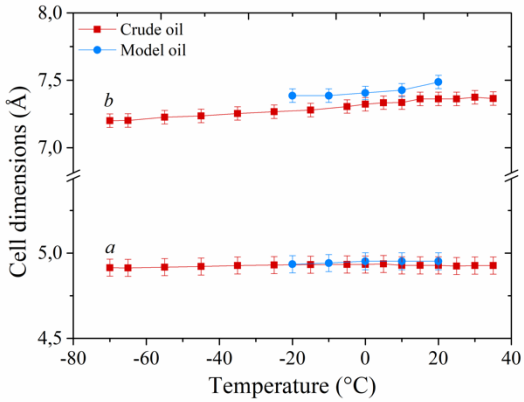

Figure 5. *Temperature dependence of the lateral unit cell parameters a and b for the crude oil and the model oil.*

At small angles, and below the WAT, the X-ray scattering spectra in **Figure 4** show one peak for the crude oil and two (harmonic) peaks for the model oil located at different positions depending on the oil and temperature. They are indexed as the (002) – and (004) – Bragg peaks of the orthorhombic unit cell[44,45] and are related to the spacing between perpendicular planes to the chains axes (or the *c* direction). Their positions are related to the mean length of molecular chains incorporated in crystals. Indeed, the simple relation $c\ (Å) = 2\ d_{002} = 2.544\ \overline{n_{RX}} + 3.75$ has been proposed, where $\overline{n_{RX}}$ stands for the mean carbon atom number chain incorporated into crystals[35,38,47]. For the crude oil, at 20 °C, $\overline{n_{RX}}$ is 50, while for the model oil, at the same temperature, $\overline{n_{RX}}$ is 27. These results highlights the differences in the *n*-paraffins distribution of the two oils.

The previous relation is valid for several situations[26] including the pure alkane phases up to solid solutions for *n*-alkane mixture of a low carbon atom number polydispersity σ of 1.5. For larger polydispersity ($3 < \sigma < 4.4$), $\overline{n_{RX}}$ is one or two unity larger than the prevalent carbon number in the mixture. For even more polydisperse synthetic waxes ($\sigma = 5.8$), three different solid solutions are identified at room temperature and disappear upon melting. The high temperature solid solution crystallizes chains with mean carbon atom number $\overline{n_{RX}}$ much larger than the prevalent carbon atom number $\overline{n}$ of synthetic wax ($\overline{n_{RX}} - \overline{n} = 7$). At the opposite, the low temperature solid solution crystallize chains shorter than the prevalent one ($\overline{n_{RX}} - \overline{n} = 2$).

By analogy, we could infer, from the polydispersities of the model oil and crude oil, that the former will crystallize in a single solid solution whereas the latter will crystallize in several solid solutions.

3.2.2. Surface to volume $[S/V]_{SAXS}$ ratios

At small q values, the crude oil spectra (**Figure 4a**) show a significant scattering signal at high temperatures (above the WAT) while the model oil spectra (**Figure 4b**) present a flat signal. The flat signal is related to a 'true' liquid (*i.e.* an assembly of small molecules) whereas the q dependent signal is associated with electronic density fluctuations at ~ q^{-1} length scale. Such upturn of scattering intensity at small q values has already been noticed on de-asphalted crude oils[48,49] without any further investigations on the nature of such fluctuations. The crude oil subtracted curves (**Figure 6a**) show a first regime at low q with a q^{-2} dependence and a second one at large q following a q^{-4} power law. The q^{-4} dependence (Porod domain) allows to estimate the surface to volume $[S/V]_{SAXS}$ ratio according to the equation (3). The surface to volume $[S/V]_{SAXS}$ values are plotted in **Figure 7a**. Values are quite high, in the range of 10^5 - 10^6 cm^{-1}, and vary in the same way as the crystal content as a function of temperature. For the model oil, we observe a q^{-4} power law in the whole q range (**Figure 6b**).

As for the crude oil, this *Porod* regime allows to estimate the surface to volume $[S/V]_{SAXS}$ ratios (**Figure 7b**). The surface to volume $[S/V]_{SAXS}$ ratios vary in the same way as the crystal content but their values, 0.8 to 2.10^3 cm^{-1}, are three decades lower than for the crude oil.

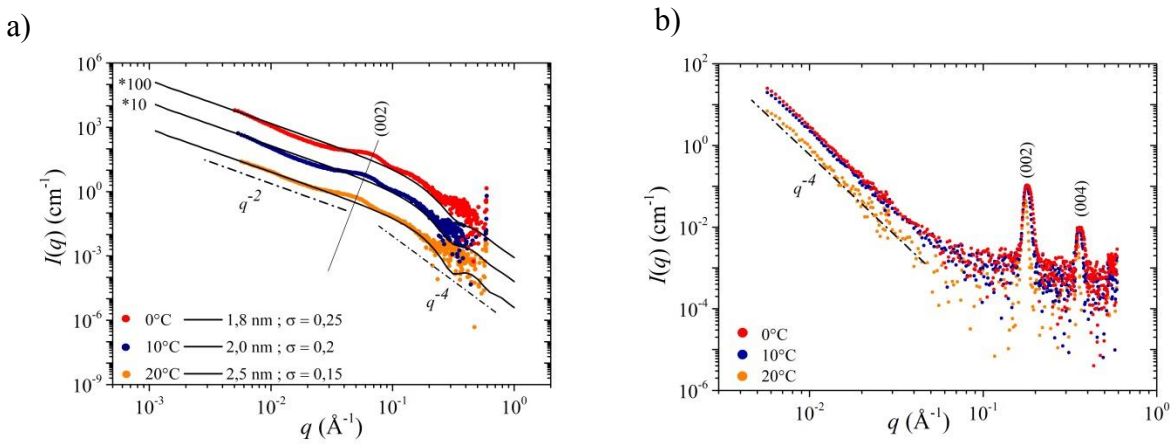

Figure 6 . *a) crude oil and b) model oil SAXS spectra from Figure 4 subtracted from solvent and normalized by the sample volume fraction. The solid lines in Figure 6a correspond to the fit of a flat disc model of variable polydisperse thickness.*

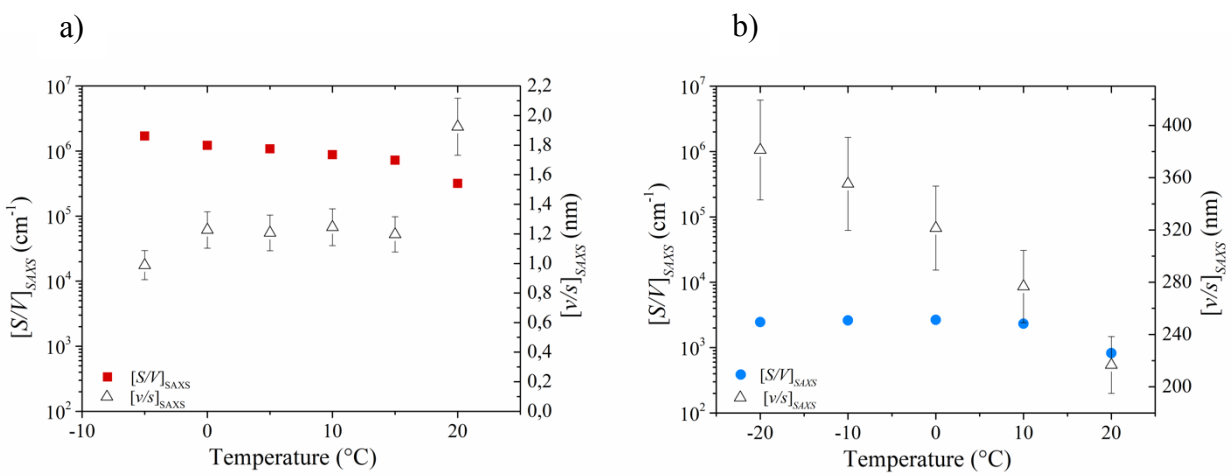

Figure 7. *Surface to volume $[S/V]_{SAXS}$ and volume to surface $[v/s]_{SAXS}$ ratios obtained from SAXS measurements for a) the crude oil and b) the model oil.*

3.2.3. Crystals form

The q^{-2} behavior observed on the crude oil spectra (**Figure 6a**) is reminiscent of 2D objects such as discs or lamellae.

3.2.4. Crystals size

The crystal size domain in direction *a* or *b* perpendicular to chain axis, is related to the width of the (hk0) peak at half height. For the two oils, the measured widths of the (110) peak are in the same order of magnitude as the instrument resolution (**Figure 8**). It means that the crystal size domains, in the crude oil and the model oil, are larger than ≈ 1000 Å in direction *a* and *b*. So, in the directions perpendicular to chain axis, crystals show a long-range order.

Then, (00*l*) reflections can be used to measure the crystals size domains in the direction of the chains on the whole range of temperature for the model oil and just below the WAT for the crude oil. For the two oils, the measured widths of the (002) peak do not have the same order of magnitude as the instrument resolution (**Figure 8**). The maximum crystallite size, in direction *c*, is found to be of the order of 160 Å in the crude oil and 1200 Å in the model oil. These sizes are typical of anisotropic objects, which is in good agreement with lamellar crystals.

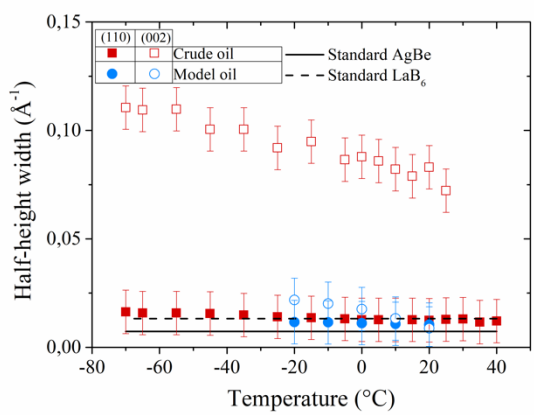

Figure 8. *Half-height width of the peaks (110) and (002) of the crude oil and model oil as a function of temperature.*

For flat particles of thickness *2H*, the volume to surface ratio [*v/s*] of one particle is simply *2H*, and could be obtained from the total surface to volume $[S/V]_{SAXS}$ ratio and the volume fraction ϕ (equation (5)). For the crude oil, *2H=v/s* are plotted as a function of temperature on **Figure 7a**.

The *2H* values are quite small, in the range of monomolecular thickness, and seems rather constant in the studied temperature range, suggesting that each new crystal formed has a monomolecular thickness[20,28,50]. To confirm this thickness and since the interactions between particles are not probed in the observed *q* range, the whole SAXS patterns are fitted to flat discs form factor (equations are described in supplementary information **f**). The results (**Figure 6a**) indicate a mean thickness of 2-3 nm, which is in good agreement with the thickness deduced from the surface to volume $[S/V]_{SAXS}$ ratios. So, in the direction of chain axes, crystals from the crude oil develop a very short range order.

The cross over point, q^*, defined as $q^* = 1/2H$, between the q^{-2} and q^{-4} behavior can also be used to estimate directly the thickness *2H* of the particles. From the *Porod* regime observed in the model oil spectra (**Figure 6b**), it is possible to obtain a minimum value of $2H_{min}$ ($2H_{min} > 1/q_{min}$) for the model oil. The minimum value of $2H_{min}$ found is approximately 160 Å.

If we assume, as suggested by CPM and Bragg peak broadening observations, that model oil particles are lamellae, we can also estimate the crystal thickness $2H=v/s$ (**Figure 7b**). Their values increases slightly as temperature decrease but we can retain an average value of $2H_{(v/s)} \approx$ 3000 Å. This thickness is *(i)* larger than the crystal size domain (1200 Å) highlighting likely the stacking default in the chain axis direction, *(ii)* smaller than the CPM observation that is also questionable in respect to parallax effects and to resolution, *(iii)* greater than the minimum value of $2H_{min}$ found. Anyway, the lamella thickness for the model oil is 2-3 order of magnitude larger than for the crude oil showing a longer-range order.

3.3. Fluid dynamics within the crystals network

Information about the fluid dynamics, its state of confinement within the crystal network formed are extracted from NMR results.

The T_2 distribution curves obtained at few temperatures, from above the WAT detected by DSC (51 °C and 22°C) to below the WAT, for the two oils **(**after the multi-component decomposition) are shown on **Figure 9**. Concerning the crude oil, as the amount of crystals is low between 51 °C and 31 °C, NMR detects the appearance of crystals and a change in behavior at a temperature $T_{crystals}$ = 30 °C. For the model oil, the change in behavior and the appearance of the crystals coincide with the WAT detected by DSC ($T_{crystals}$ = 22 °C).

Above $T_{crystals}$, the T_2 distributions show a main peak with high T_2 values (**Figure 9**). For the crude oil, the peak is wide and asymmetrical, while for model oil it is thin and symmetrical. The asymmetrical distribution shape of the peak has already been observed on de-asphalted crude oil[51] and is probably due to the presence of objects in the liquid phase which are remaining above the WAT, as observed on the crude oil SAXS spectra (section 3.2.2).

As the temperature decreases, the two oils show similar behaviors since the main peak shifts to shorter T_2 and expands. The shift and expansion are caused by an increase of the bulk oil viscosity with the temperature and by the formation of surfaces magnetic relaxations that appear during crystallization.

Below $T_{crystals}$, the crude oil results show the presence of a visible shoulder and peaks at short T_2 that does not exist in the model oil. The shoulder intensity increases and the intensity of the main peak decreases as the temperature decreases. These behaviors can be related to SAXS results and reflect a high quantity of surfaces formed (**Figure 7**, section 3.2.2) and a reduction in the bulk oil protons mobility, which is more significant in the crude oil compared with the model oil. From these observations, we can assume that there are two different protons populations with different mobility, which interact with the surfaces created during crystals formation. They interact with

two different environments and with different characteristics, including different solvent domain sizes.

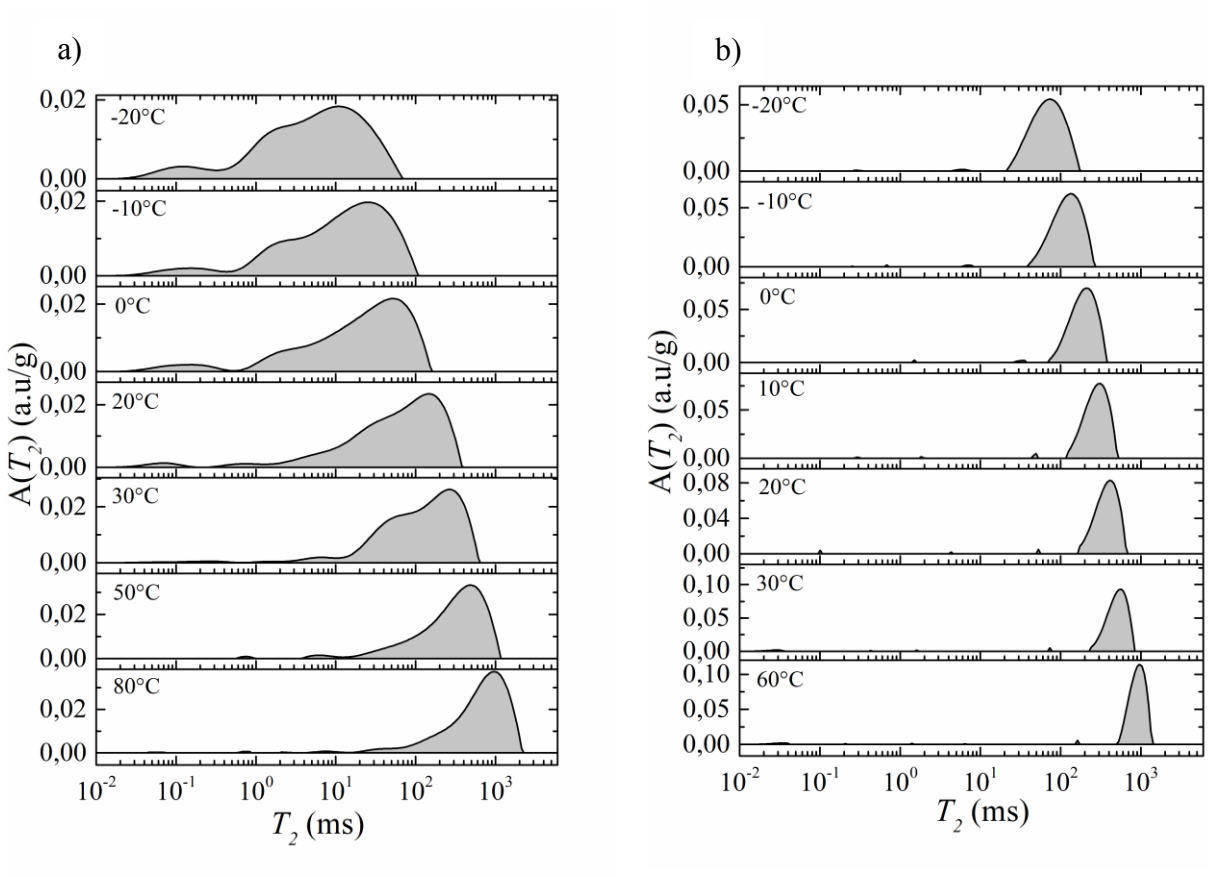

Figure 9. *Relaxation time distributions, plotted as the log relaxation time versus the normalized signal intensity, at different temperatures for a) the crude oil and b) the model oil. The relaxation time distributions shown were obtained at an echo time of 100 μs.*

3.3.1. NMR sensitivity to crystals surfaces

We are now interested in the crude oil and model oil main peak evolution present at large T_2 as the temperature decreases (**Figure 10**). We considered the maximum of the distribution as a tracer of T_2 evolution.

Above $T_{crystals}$, the function $ln(T_2)$ varies linearly with the inverse of the temperature. A straight line is drawn to show this evolution. When the temperature decreases, T_2 decreases until $T_{crystals}$

and then deviates from this first line. This deviation is due to the creation of crystals and new surfaces relaxation. To confirm that, measurements on oil 20 and oil 5 were conducted above their WAT. The results show that the T_2 obtained are in line with the T_2 of the crude oil obtained at $T > T_{crystals}$ and confirm that the deviation is due to the formation of surfaces in the mixture (**Figure 10**).

Protons of the liquid phase are now interacting with the spins of surfaces. It can be noticed that the deviation is more important for the crude oil than for the model oil, due to the large amount of surfaces areas present in the crude oil as observed with SAXS/WAXS results (**Figure 7**, section 3.2.2).

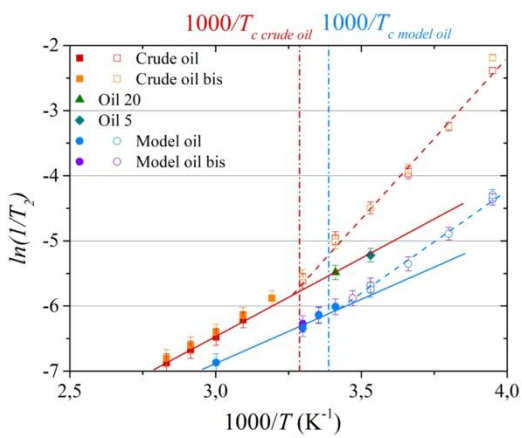

Figure 10. *Evolution of the main peak relaxation rate obtained, from the multi-components distributions, versus the inverse of temperature for the crude oil and the model oil. "Bis" refers to a repetition of a set of measurements.*

3.3.2. Confined and unconfined liquid

Then, to go further in understanding the dynamic process and proton populations associated with this system, we focused only on the main peak and its shoulder by decomposing the T_2 distributions into only two components. The first three points of the distributions were removed in order to only take into account the contribution of the liquid which relaxes at $T_2 > 0.1$ ms

(supplementary information **e**). The two-components decomposition is carried out at all temperatures below $T_{crystals}$. An example of the decomposition and a fit with a lognormal distribution, on the signal at 0 °C, is represented on **Figure 11**. The main peak is represented by the decomposition (1) and the shoulder by the decomposition (2).

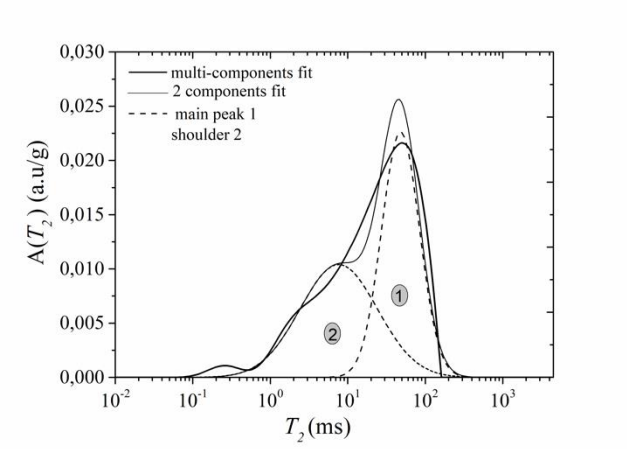

Figure 11. *The crude oil relaxation time distribution obtained at 0°C with a multi-component fit (dark solid line) and a two-component fit (light solid line). The two-component distribution (light solid line) is decomposed into two peaks (dashed line): the main peak represented by component (1) and the shoulder represented by component (2).*

The peaks proportion evolution was studied to characterize the exchanges that can take place between the two peaks and have more information on the behavior of each proton population as the temperature decreases (**Figure 12**). The two-components fit gives the proportion of the main peak and the shoulder associated with the measured magnetization $M_{measured}$. The total proportion of the main peak and shoulder (1+2) corresponds to the ratio between the magnetization measured after decomposition into two components and the magnetization extrapolated by the Curie's law [$M_{measured}/M_{extrapolated}$].

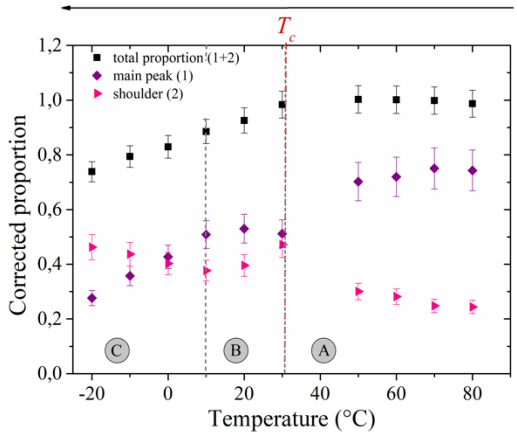

Figure 12. *Corrected proportions of extrapolated magnetization attributed to the main peak and shoulder as a function of temperature (see text for detailed explanation). A,B,C represent the different behavior observed. These behaviors are explained in the text.*

On **Figure 12**, we can notice that the shoulder is pre-existing at high temperatures and its proportion is not negligible (≈ 20 %). Three regimes can be distinguished when the temperature decreases:

- In the first regime A (T> $T_{crystals}$), the total proportion remains constant and we observe an increases of the shoulder proportion (2) while the proportion of the main peak (1) decreases. This can be related to the *n*-paraffins molecules that are less and less mobile.
- In the transition regime B (T < $T_{crystals}$), the main peak proportion (1) stays stable, the shoulder proportion (2) slightly decreases and the total decreases. This is due to the creation of *n*-paraffins crystals. Indeed, a part of protons initially associated to the shoulder are now incorporated in solids.
- In the final regime C (T<< $T_{crystals}$), the total and main peak proportion (1) decreases whereas the shoulder proportion (2) increases. There is an important part of the main peak proton population (1) which is now associated with the shoulder protons environment. This means that in addition to the creation of crystals, there is also a lot of new surfaces created. This observation is consistent with $[S/V]_{SAXS}$ SAXS results.

These observations confirm that between the two population of protons identified by NMR, the main peak corresponds to a liquid less confined than the one represented by the shoulder. Therefore, to go further, one would like to evaluate the liquid distances between the surfaces associated with these two proton populations identified. From the surface to volume $[S/V]_{SAXS}$ ratio values obtained a mean liquid distance over the entire sample d_{mean} can be obtained from equation (7) :

$$d_{mean} = \frac{1}{\left[\frac{S}{V}\right]_{SAXS}\left(\frac{1}{(1-\phi)}\right)} \tag{7}$$

The values of d_{mean} obtained (**Figure 13**) are on the order of few nanometers. However, as an order of magnitude, the chain length of an *n*-paraffin molecule containing 15 carbons is 4 nm, which is of the same order of magnitude as d_{mean}. This means that the liquid is very confined with few or no bulk volume and there is mostly adsorption of the molecules on surfaces. In this case, the fast exchange model is not valid. Thus, the distances associated with each protons population cannot be determined from the equation (1) and surface to volume [*S/V*] ratios obtained by NMR and SAXS as presented in supplementary information **f**.

Ongoing studies could thus focus on further information about the two protons population identified. On the one hand, at large scale, the exchange dynamics between the different proton populations could be investigated by (2D) NMR T_2-Δ-T_2[52]. On the other hand, it would be interesting to probe by NMRD[53] the local interfacial dynamics of these protons populations in these pronounced confinements.

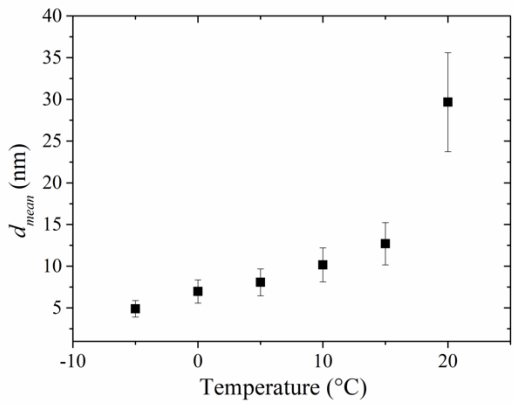

Figure 13. *Liquid distances between surfaces d_{mean} estimated from SAXS measurements as a function of temperature.*

4. DISCUSSIONS AND CONCLUSIONS

In the current study, we focused on *n*-paraffins crystallization to probe at multi length-scale the *n*-paraffins structure and the behavior of the liquid within the crystal network formed during crystallization. A multi modal strategy was proposed including CPM, SAXS/WAXS and low field NMR experiments. Two waxy oils, a crude oil and a model oil, of different *n*-paraffins polydispersities and compositions were used. The major results of the study are summarized in **Table 4** below.

Table 4. *Summary of the major results (n.d = not determined).*

	n-paraffins polydispersity σ	Crystalline structure	Crystals thickness (nm)	Crystals shape	$[S/V]_{SAXS}$ (cm^{-1})	Liquid distance d_{mean} (nm)
Crude oil	>7.2	Orthorhombic	1-10	Lamellar	$\approx 10^6$	5-30
Model oil	2.1	Orthorhombic	> 120	Lamellar	$\approx 10^3$	n.d

Above the WAT, no structure should subsist since the *n*-paraffins are totally solubilized. Though, no singular behavior is observed for the model oil. The results obtained with the crude oil by SAXS and NMR revealed the presence of molecules at high temperatures with a distinct signature, which were unobservable by CPM. Asphaltenes but also other complex molecules could be at the origin of such behavior as reported in the literature on de-asphalted crude oils[48,51].

More investigations, out of the scope of the present paper, could be performed to probe which molecules are responsible for this peculiar signature.

Below the WAT, *n*-paraffins crystals appear. In the model oil, crystals form a single solid solution with an orthorhombic structure. In the crude oil, several solid solutions with an orthorhombic structure are formed. In both cases, the cell parameters are about a = 7.40 Å ± 0.05 Å and b = 4.92 Å ± 0.05 Å. The *n*-paraffins crystals size is about 1-10 nm in the crude oil and larger than 120 nm in the model oil. These differences in size could be due to the presence of non-crystallizable molecules such as isoalkanes or cycloalkanes, resins and asphaltenes, which inhibit crystal development and promote the formation of small structures [54–56]. A high concentration of resin-type molecules can lead to aggregates of poorly crystallized forms that grow following a branch-like shape. As crystals grow, they change direction because the localized accumulation of impurities on surfaces promote the formation of branches[56]. Studies on long *n*-paraffin chains and semi-crystalline polymers have also shown that the structure of crystal aggregates depends on the applied undercooling ($\Delta T = T - T_c$ with T_c the crystallization temperature)[57]. At low degree of undercooling the crystal aggregates will be more hedritic in shape and at larger degree of undercooling the branches will divide more and more and the shape of the aggregate will tend more towards spherulites, which are a set of thin lamellae organized in spherical and symmetrical macrostructures[43]. These conclusions drawn from the literature can be compared with the results we obtained in this study. Indeed, SAXS measurements showed that the formed crystals have a lamellar shape. Thus, we can deduce from the model oil CPM images that the observed platelets composed of a stack of lamellae are in fact aggregates of crystals of lamellar shape. As observed in the literature[43,56], we could expect that they grow in branched form with branches that divide more and more as the temperature decreases. However, since the

model oil does not contain asphaltenes and resins, the crystals are larger and the branches divide significantly less than in the crude oil (**Figure 14**). This observation can be supported looking at the evolution of trapped liquid protons population identified in the crude oil and unobservable in the model oil: the more branches, the greater the amount of liquid trapped between the branches. Future NMR studies could give more information about the dynamics of these trapping liquid areas. Furthermore, it is worth to notice that during the formation of the branched *n*-paraffins crystals, liquid is trapped and the effective volume of the system (crude oil + crystals) occupies a larger volume than the net volume occupied by the crystals packed together. This effective volume fraction, which is considered when modeling the gelled waxy crude oil as a suspension of fractal aggregates, would be an interesting data to refine or discriminate the existing rheological models[6,7,58].

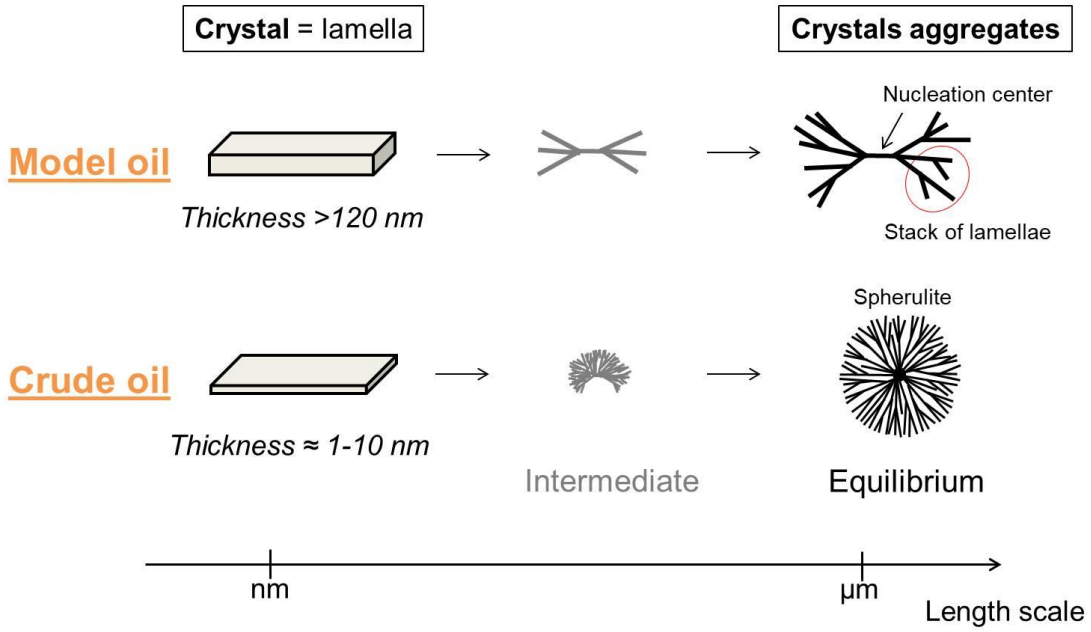

Figure 14. *Illustration of the aggregation process of n-paraffins crystals in (a) model oil and (b) crude oil.*

5. ACKNOWLEDGEMENT

The authors are grateful to IFP Energies nouvelles, PHENIX laboratory and TOTAL for their financial and scientific support. The authors thank J. M'hamdi (IFPEN) for his help in setting up SAXS/WAXS experiments. The authors extend sincere thanks to I. Hénaut (IFPEN) for the interesting discussion about DSC measurements and interpretation of results. We would like to thank the referees for their careful reading of the manuscript. They have enabled us to clarify the presentation of our work and to significantly improve the manuscript. All authors contributed to the discussion, the writing and the review of this paper.

6. SUPPORTING INFORMATION

The procedure followed to determine the WAT and the WPC is given in supplementary information as well as densities and elemental composition of the oils. Equations used to calculate σ and $\bar{n}$ parameters can be found in supplementary data. The experimental protocol of the temperature-controlled centrifugation is also given. SAXS/WAXS theoretical background are given in supplementary information. For the crude oil, the magnetization evolution measured by NMR and the methodology followed to calculate the distances between the confined liquid and the surfaces created during crystallization are also detailed.

7. REFERENCES

(1) Merino-Garcia, D.; Margarone, M.; Correra, S. Kinetics of Waxy Gel Formation from Batch Experiments. *Energy Fuels* **2007**, *21*, 1287–1295.

(2) Rønningsen, H. P. Production of Waxy Oils on the Norwegian Continental Shelf: Experiences, Challenges, and Practices. *Energy Fuels* **2012**, *26*, 4124–4136.

(3) Soedarmo, A. A.; Daraboina, N.; Lee, H. S.; Sarica, C. Microscopic Study of Wax Precipitation—Static Conditions. *Energy Fuels* **2016,** DOI: 10.1021/acs.energyfuels.5b02653.

(4) Soedarmo, A. A.; Daraboina, N.; Sarica, C. Validation of wax deposition models with recent laboratory scale flow loop experimental data. *Journal of Petroleum Science and Engineering* **2017**, *149*, 351–366.

(5) Pedersen, K. S.; Rønningsen, H. P. Effect of Precipitated Wax on Viscosity - A Model for Predicting Non-Newtonian Viscosity of Crude Oils. *Energy Fuels* **2000**, *14*, 43–51.

(6) Palermo, T.; Tournis, E. Viscosity Prediction of Waxy Oils: Suspension of Fractal Aggregates (SoFA) Model. *Ind. Eng. Chem. Res.* **2015**, *54*, 4526–4534.

(7) Li, H. A generalized model for predicting non-Newtonian viscosity of waxy crudes as a function of temperature and precipitated wax. *Fuel* **2003**, *82*, 1387–1397.

(8) Mendes, R.; Vinay, G.; Ovarlez, G.; Coussot, P. Reversible and irreversible destructuring flow in waxy oils: An MRI study. *Journal of Non-Newtonian Fluid Mechanics* **2015**, *220*, 77–86.

(9) Chang, C.; Nguyen, D.Q.; Rønningsen, H. P. Isothermal start-up of pipeline transporting waxy crude oil. *J.Non-Newtonian Fluid Mech* **1999**, *87*, 127–154.

(10) Wachs, A.; Vinay, G.; Frigaard, I. A 1.5D numerical model for the start up of weakly compressible flow of a viscoplastic and thixotropic fluid in pipelines. *Journal of Non-Newtonian Fluid Mechanics* **2009**, *159*, 81–94.

(11) Fogler, H.S.; Zheng, S.; Huang, Z. Experimental Characterization of Important Wax Thermodynamic Properties. In *Wax deposition: Experimental characterizations, theoretical modeling, and field practices*; Huang, Z., Zheng, S., Fogler, H. S., Eds.; Emerging trends and technologies in petroleum engineering; CRC Press Taylor & Francis Group: Boca Raton, 2015; pp 9–40.

(12) Alcazar-Vara, L.A.; Buenrostro-Gonzalez, E. Characterization of the wax precipitation in Mexican crude oils. *Fuel Processing Technology* **2011**, *92*, 2366–2374.

(13) Roenningsen, H.S.; Bjoerndal, B.; Hansen, A.B.; Pedersen, W.B. Wax precipitation from North Sea crude oils: 1. Crystallization and dissolution temperatures, and Newtonian and non-Newtonian flow properties. *Energy Fuels* **1991**.

(14) Létoffé, J. M.; Claudy, P.; Kok, M. V.; Garcin, M.; Volle, J. L. Crude oils : characterization of waxes precipitated on cooling by d.s.c and thermomicroscopy. *Fuel* **1995**, *74*, 810–817.

(15) N. F Dandah and D. A. Wavrek. Characterization of High-Molecular-Weight Paraffin in Ordovician Simpson Group Reservoirs (Oklahoma and Texas)—Implications for Advanced Recovery Technologies. *Oklahoma Geological Survey Circular* **1997**, *99*.

(16) Aquino Neto, F.R. de; Cardoso, J.N.; dos Santos Pereira, A.; Fernandes, M. C. Z.; Caetano, C.A.; Castro Machado, A.L. de. Application of high temperature high resolution gas chromatography to paraffinic deposits in petroleum production pipelines. *J. High Resol. Chromatogr.* **1994**, *17*, 259–263.

(17) Hong, Z.; Guanghui, H.; Cuishan, Z.; Peirong, W.; Yongxin, Y. The quantitation and origin of C40+ n-alkanes in crude oils and source rocks. *Organic Geochemistry* **2003**, *34*, 1037–1046.

(18) Holder, G. A.; Winkler, J. Wax Crystallization from Distillate Fuels: II. Mechanism of Pour Depression. *J. Inst. Petrol.* **1965**, 51–228.

(19) Srivastava, S. P.; Tandon R.S; Verma P.S; Saxena, A.K.; Joshi, G.C.; Phatak, S.D. Crystallization behaviour of n-paraffins in Bombay-High middle-distillate wax/gel. *Fuel* **1992**, *71*, 533–537.

(20) Kané, M.; Djabourov, M.; Volle, J. L.; Lechaire, J. P.; Frebourg, G. Morphology of paraffin crystals in waxy crude oils cooled in quiescent conditions and under flow. *Fuel and Energy Abstracts* **2003**, *44*, 290–291.

(21) Ruffier-Meray V.; Roussel, J.-C.; Défontaines, A.-D. Use of pulsed NMR spectroscopy to measure the amount of solid in waxy crudes. *Institut Français du Pétrole* **1998**, *53*.

(22) Freed, D. E. Dependence on chain length of NMR relaxation times in mixtures of alkanes. *The Journal of chemical physics* **2007**, *126*, 174502.

(23) Ruwoldt, J.; Humborstad Sørland, G.; Simon, S.; Oschmann, H.-J.; Sjöblom, J. Inhibitor-wax interactions and PPD effect on wax crystallization: New approaches for GC/MS and NMR, and comparison with DSC, CPM, and rheometry. *Journal of Petroleum Science and Engineering* **2019**, *177*, 53–68.

(24) Dirand, M.; Chevallier, V.; Provost, E.; Bouroukba, M.; Petitjean, D. Multicomponent paraffin waxes and petroleum solid deposits : structural and thermodynamic state. *Fuel* **1998**, *77*, 1253–1260.

(25) Dirand, M.; Bouroukba, M.; Chevallier, V.; Petitjean, D.; Behar, E.; Ruffier-Meray V. Normal Alkanes, Multialkane Synthetic Model Mixtures, and Real Petroleum Waxes: Crystallographic Structures, Thermodynamic Properties, and Crystallization. *J. Chem. Eng. Data* **2002**, *47*, 115–143.

(26) Petitjean, D.; Schmitt, J. F.; Laine, V.; Cunat, C.; Dirand, M. Influence of the Alkane Molar Distribution on the Physical Properties of Synthetic Waxes. *Energy Fuels* **2010**, *24*, 3028–3033.

(27) Polacco, G.; Filippi, S.; Paci, M.; Giuliani, F.; Merusi, F. Structural and rheological characterization of wax modified bitumens. *Fuel* **2012**, *95*, 407–416.

(28) Paso, K.; Senra, M.; Yi, Y.; Sastry, A. M.; Fogler, H. S. Paraffin Polydispersity Facilitates Mechanical Gelation. *Ind. Eng. Chem. Res.* **2005**, *44*, 7242–7254.

(29) Venkatesan, R.; Nagarajan, N. R.; Paso, K.; Yi, Y.-B.; Sastry, A. M.; Fogler, H. S. The strength of paraffin gels formed under static and flow conditions. *Chemical Engineering Science* **2005**, *60*, 3587–3598.

(30) G. Cazaux; L. Barre; F. Brucy; Institut Français du Petrole. Waxy Crude Cold Start: Assessment Through Gel Structural Properties. *SPE* **1998**, 729–739.

(31) Hennessy, A.; Neville, A.; Roberts, K. J. In-Situ SAXS/WAXS and Turbidity Studies of the Structure and Composition of Multihomologous n -Alkane Waxes Crystallized in the Absence and Presence of Flow Improving Additive Species. *Crystal Growth & Design* **2004**, *4*, 1069–1078.

(32) Radlinski, A.P.; Barré, L.; Espinat, D. Aggregation of n-alkanes in organic solvents. *Journal of Molecular Structure* **1996**, 51–56.

(33) Korb, J.-P.; Vorapalawut, N.; Nicot, B.; Bryant, R. G. Relation and Correlation between NMR Relaxation Times, Diffusion Coefficients, and Viscosity of Heavy Crude Oils. *J. Phys. Chem. C* **2015**, *119*, 24439–24446.

(34) Ruwoldt, J.; Kurniawan, M.; Oschmann, H.-J. Non-linear dependency of wax appearance temperature on cooling rate. *Journal of Petroleum Science and Engineering* **2018**, *165*, 114–126.

(35) Chevallier, V.; Provost, E.; Bourdet, J.B.; Bouroukba, M.; Petitjean, D.; Dirand, M. Mixtures of numerous different n-alkanes: 1. Structural studies by X-ray diffraction at room temperature—Correlation between the crystallographic long c parameter and the average composition of multi-alkane phases. *Polymer* **1999**, *40*, 2121–2128.

(36) Small, D.M. *The Physical Chemistry of Lipids: From Alkanes to Phospholipids*; Handbook of Lipid Research 4; New-York, 1986.

(37) Jayalakshmi, V.; Selvavathi, V.; Sekar, M. S.; Sairam, B. Characterisation of Paraffin Waxes by DSC and High Temperature GC. *Petroleum Science and Technology* **1999**, *17*, 843–856.

(38) Chevallier, V.; Briard, A. J.; Petitjean, D.; Hubert, N.; Bouroukba, M.; Dirand, M. Influence of the Distribution General Shape of n-Alkane Molar Concentrations on the Structural State of Multi-Alkane Mixtures. *Molecular Crystals and Liquid Crystals Science and Technology. Section A. Molecular Crystals and Liquid Crystals* **2000**, *350*, 273–291.

(39) Berne, P.; Bachaud, P.; Fleury, M. Diffusion Properties of Carbonated Caprocks from the Paris Basin. *Oil Gas Sci. Technol. – Rev. IFP* **2010**, *65*, 473–484.

(40) Keating, K.; Knight, R. The effect of spatial variation in surface relaxivity on nuclear magnetic resonance relaxation rates. *GEOPHYSICS* **2012**, *77*, E365-E377.

(41) Taché, O.; Rouzière, S.; Joly, P.; Amara, M.; Fleury, B.; Thill, A.; Launois, P.; Spalla, O.; Abécassis, B. MOMAC: A SAXS/WAXS laboratory instrument dedicated to nanomaterials. *J Appl Crystallogr* **2016**, *49*, 1624–1631.

(42) Shaffer, L. B.; Hendricks, R. W. Calibration of polyethylene (lupolen) as a wavelength-independent absolute intensity standard. *J Appl Crystallogr* **1974**, *7*, 159–163.

(43) Crist, B.; Schultz, J. M. Polymer spherulites: A critical review. *Progress in Polymer Science* **2016**, *56*, 1–63.

(44) Briard, A.-J.; Bouroukba, M.; Petitjean, D.; Hubert, N.; Moïse, J.-C.; Dirand, M. Thermodynamic and structural analyses of the solid phases in multi-alkane mixtures similar to petroleum cuts at ambient temperature. *Fuel* **2005**, *84*, 1066–1073.

(45) Chevallier, V.; Petitjean, D.; Bouroukba, M.; Dirand, M. Mixtures of numerous different n-alkanes: 2. Studies by X-ray diffraction and differential thermal analyses with increasing temperature. *Polymer* **1999**, *40*, 2129–2137.

(46) Ungar, G.; Masic, N. Order in the rotator phase of n-alkanes. *J. Phys. Chem. C* **1985**, *89*, 1036–1042.

(47) Rakotosaona, R.; Bouroukba, M.; Petitjean, D.; Dirand, M. Solubility of a Petroleum Wax with an Aromatic Hydrocarbon in a Solvent. *Energy Fuels* **2008**, *22*, 784–789.

(48) Eyssautier, J.; Hénaut, I.; Levitz, P.; Espinat, D. Barré, L. Organization of Asphaltenes in a Vacuum Residue: A Small-Angle X-ray Scattering (SAXS)–Viscosity Approach at High Temperatures. *Energy Fuels* **2011**, *26*, 2696–2704.

(49) Headen, T. F.; Boek, E. S.; Stellbrink, J.; Scheven, U. M. Small angle neutron scattering (SANS and V-SANS) study of asphaltene aggregates in crude oil. *Langmuir : the ACS journal of surfaces and colloids* **2009**, *25*, 422–428.

(50) Chichakli, M.; Jessen, F. W. Crystal Morphology in Hydrocarbon Systems. *Industrial and engineering chemistry* **1967**, 86–98.

(51) Vorapalawut, N.; Nicot, B. Louis-Joseph, A.; Korb, J.-P. Probing Dynamics and Interaction of Maltenes with Asphaltene Aggregates in Crude Oils by Multiscale NMR. *Energy Fuels* **2015**, *29*, 4911–4920.

(52) McDonald, P. J.; Korb, J.-P.; Mitchell, J.; Monteilhet, L. Surface relaxation and chemical exchange in hydrating cement pastes: A two-dimensional NMR relaxation study. *Phys. Rev. E* **2005**, *72*, 623.

(53) Levitz, P. Probing interfacial dynamics of water in confined nanoporous systems by NMRD. *Molecular Physics* **2018**, *117*, 952–959.

(54) Xue, H.; Zhang, J.; Han, S.; Sun, M.; Yan, X.; Li, H. Effect of Asphaltenes on the Structure and Surface Properties of Wax Crystals in Waxy Oils. *Energy Fuels* **2019**, *33*, 9570–9584.

(55) Garcia, M.C.; Carbognani L.; Orea, M.; Urbina, A. The influence of alkane class-types on crude oil wax crystallization and inhibitors efficiency. *Fuel and Energy Abstracts* **2000**, *41*, 352.

(56) Birdwell, B. F. Crystallization of petroleum waxes. *Nature* **1966**, *209*, 366–368.

(57) Teckoe, J.; Bassett, D.C. The crystallization kinetics of monodisperse C98H198 from the melt. *Polymer* **2016**, *41*, 1953–1957.

(58) Pedersen, K. S.; Rønningsen, H. P. Effect of Precipitated Wax on Viscosity A Model for Predicting Non-Newtonian Viscosity of Crude Oils. *Energy Fuels* **2000**, *14*, 43–51.